1 Word count: 9,470

2 **REVISION 3 Barium Mobility in a Geothermal Environment, Yellowstone National Park**

3 Jarred Zimmerman[1] and Peter B. Larson[1]

4 [1]School of the Environment, Washington State University, Pullman, WA 99164-2812

5

6 **ABSTRACT**

7 Ba-rich minerals are frequently observed in epithermal environments and include characteristic

8 phases such as barite and alunite supergroup minerals. At Yellowstone, in-situ EPMA-WDS

9 show that Ba in the unaltered third-cycle Tuff of Sulphur Creek is largely contained within

10 sanidine phenocrysts (mean 1.60 wt% BaO) with lesser concentrations in plagioclase (mean 0.22

11 wt% BaO) and volcanic glass (mean 0.05 wt% BaO). Whole-rock XRD analyses of rocks

12 hydrothermally altered by alkaline-chloride fluids at Ridge 7741 in Seven Mile Hole,

13 Yellowstone National Park, show they are dominated by illite + quartz ± hydrothermal feldspar,

14 primarily adularia. In this alteration zone, adularia is the principal phase that contains significant

15 Ba (mean 0.43 wt% BaO). In shallower alteration, dominated by acid-sulfate assemblages, such

16 as kaolinite + opaline silica ± alunite supergroup minerals (alunite, walthierite, huangite) ±

17 barite, Ba is sequestered in the sulfate minerals. Alunite supergroup minerals (mean 1.12 wt%

18 BaO) are more prevalent than barite and are largely found from the modern valley rim to about

19 60m below the modern surface, especially around the South Fork of Sulphur Creek. However,

20 nearly 80 m below the modern rim of the Grand Canyon of the Yellowstone River, in areas

21 previously altered by alkaline-chloride fluids, adularia altered to alunite supergroup minerals

22 may contain similar to slightly elevated Ba concentrations relative to the replaced grain. Barite

23 is primarily found sporadically in altered rocks along the valley rim of the South Fork of Sulphur

24   Creek, with rare occurrences along the rim of the Grand Canyon. Despite the hydrothermal

25   alteration, whole-rock XRF and ICP-MS analyses show similar mean concentrations between

26   unaltered (0.11 wt% BaO) and altered (0.09 wt% BaO) Tuff of Sulphur Creek samples.

27   Hydrothermally altered rocks are important sources of Yellowstone low $\delta^{18}O$ rhyolites, like the

28   Tuff of Sulphur Creek, which inherit their low $\delta^{18}O$ signal from them. Cenozoic rhyolites

29   throughout the North American Cordillera tend to exhibit high Ba concentrations, including the

30   low $\delta^{18}O$ Yellowstone rhyolites. This work shows that hydrothermal alteration mobilizes Ba in

31   volcanic units with minimal dispersion of Ba out of that unit. The genesis of similar silicic

32   volcanic rocks with elevated Ba, relative to mean upper crustal concentrations, may be the result

33   of partial melting of hydrothermally altered rock.

34   Keywords: epithermal, Yellowstone, barium, hydrothermal, alkaline-chloride, acid-sulfate,

35   rhyolite

36   **INTRODUCTION**

37   Barite is a common hydrothermal mineral in shallow volcanic-hosted epithermal

38   environments (Plumlee et al. 1995; White and Hedenquist 1995; Dill et al. 1997; Simmons et al.

39   2005; Vikre 2007; John et al. 2010; Piochi et al. 2015), and the hydrothermal system in the

40   Yellowstone caldera, Wyoming, is no exception to this observation (Love and Good 1970;

41   Larson et al. 2009). The mean abundance of Ba in the upper crust is about 624 ppm (Rudnick

42   and Gao 2003). Ba is highly incompatible during mantle melting which leads to upper crustal

43   enrichment (Nan et al. 2018) and, due to its solubility in aqueous fluids, can be concentrated in

44   the epithermal environment. Many Cenozoic volcanic rocks in the North American Cordillera

45   host barite-bearing epithermal deposits and contain high background concentrations of Ba (e.g.,

46   Long Hike Mine, Jarbidge mining district, Nevada (Brueseke et al. 2014); Homestake Claim,

47   Creede mining district, Colorado (Emmons and Larsen 1923; Bachmann et al. 2014)). After the

48   Oligocene "ignimbrite flare up," Basin and Range extension of the Nevadaplano in the mid-

49   Miocene drove bimodal basalt-rhyolite volcanism and renewed epithermal processes (e.g.,

50   Midas, Sleeper, Mule Canyon, all in Nevada) (John 2001; Christiansen and McCurry 2008;

51   Brueseke et al. 2014).

52   The Yellowstone rhyolites follow this Cordilleran pattern of elevated whole-rock Ba

53   concentrations. Typical rhyolites at Yellowstone have elevated Ba concentrations compared to

54   other Cenozoic rhyolites from the North American Cordillera, mean approximately 660 ppm,

55   data selected using location = bounding box approximating North American Cordillera, sample

56   type = rock name: rhyolite, age = Cenozoic (0 Ma – 65.5 Ma), material = bulk, normalization =

57   major elements as reported (http://portal.earthchem.org/, accessed Feb. 2, 2023). For example,

58   the Huckleberry Ridge Tuff contains about 1,432 ppm Ba (Bindeman and Valley 2001; Swallow

59   et al. 2019), the Tuff of Sulphur Creek has about 857 ppm (Pritchard and Larson 2012), and

60   Canyon Flow about 901 ppm (Bindeman and Valley 2001; Pritchard and Larson 2012). The

61   Tuff of Sulphur Creek and Canyon Flow are post-caldera collapse rhyolites that erupted about

62   481 ka (Christiansen 2001; Pritchard and Larson 2012) and likely represent residual melt

63   pockets, whereas the Huckleberry Ridge Tuff is a major ignimbrite that erupted from the first

64   cycle Yellowstone caldera at 2.1 Ma (Hildreth et al. 1984; Bindeman and Valley 2001;

65   Christiansen 2001; Stelten et al. 2015). In these rocks, elevated Ba concentrations are primarily

66   found in the magmatic potassium feldspars (Pritchard and Larson 2012; Swallow et al. 2019).

67   Here we present chemical data on Ba-bearing phases from the Tuff of Sulphur Creek in

68   Yellowstone National Park. Ba mobility is examined in an active epithermal environment.

69   Magmatic phenocrysts of Ba-bearing sanidine were analyzed in various altering environments in

70 addition to the secondary hydrothermal phases to show how Ba moves through the system in

71 response to the conditions of the altering fluid. Ba released during alteration of primary sanidine

72 in the Yellowstone rhyolites is then sequestered into secondary hydrothermal potassium

73 minerals. In this case, Ba does not appear to be transported any great distance. Alkaline-

74 chloride fluids deeper in the epithermal environment may limit barite formation in shallower

75 portions by limiting the amount of Ba in the fluid.

76

77 **Regional Geology**

78   The Yellowstone hydrothermal system is related to the most recent caldera eruption, but

79 the hydrothermal fluids likely flow through rocks as old as Archean crystalline basement. The

80 oldest prevolcanic rocks around the Yellowstone Plateau include Archean (3.5 to 2.5 Ga)

81 Beartooth Province granitoids and schists (Christiansen and Blank 1972; Christiansen 2001;

82 Hurwitz and Lowenstern 2014; Morgan et al. 2017). Paleozoic and Mesozoic sedimentary rocks

83 are also probably present in the subsurface. The Mississippian Madison Limestone outcrops

84 extensively north and south of the Yellowstone caldera, with other units dating back to the

85 Cambrian and as young as the Cretaceous (Christiansen and Blank 1972; Christiansen 2001;

86 Feeley 2002). Intermediate lavas, volcaniclastic rocks, and sediments of the Eocene Absaroka

87 Volcanic Supergroup are also exposed in the northern and northeastern portions of the Park

88 (Hildreth et al. 1984; Christiansen 2001; Feeley 2002). Normal faulting attributed to the Basin

89 and Range Province, which accommodates approximately an E-W extension of North American

90 crust, has been alluded to as a cause for the alignment of some Yellowstone-related volcanic

91 vents (Christiansen 2001; Smith et al. 2009; Long et al. 2018; Long 2019).

92   The Yellowstone hotspot produced three nested calderas and massive ash-fall sheets in

93   the past 2.1 Ma (Fournier 1989; Christiansen 2001; Pierce et al. 2002; Pritchard and Larson

94   2012; Hurwitz and Lowenstern 2014; Morgan et al. 2017). These ash-fall sheets are the

95   Huckleberry Ridge Tuff (2.1 Ma, 2,500 km^3) (Christiansen and Blank 1972; Hildreth et al. 1984;

96   Bindeman and Valley 2001; Christiansen 2001; Smith et al. 2009; Hurwtiz and Lowenstern

97   2014) creating an unnamed caldera, the Mesa Falls Tuff (1.3 Ma, 280 km^3) (Hildreth et al. 1984;

98   Bindeman and Valley 2001; Christiansen 2001; Smith et al. 2009; Rivera et al. 2017; Morgan et

99   al. 2017; Stelten et al. 2018) creating the 15 km x 30 km Henrys Fork caldera, and Lava Creek

100   Tuff (0.63 Ma, 1,000 km^3) (Matthews et al. 2015; Rivera et al. 2017; Morgan et al. 2017; Troch

101   et al. 2018; Till et al. 2019) creating the 80 x 50 km Yellowstone caldera which is wholly

102   contained in the boundaries of Yellowstone National Park (Hildreth et al. 1984; Christiansen

103   2001; Hurwitz and Lowenstern 2014). The nested calderas create a complex stretching from

104   southeastern Idaho to northwestern Wyoming (Fig 1).

105   Each volcanic cycle is composed of pre-collapse rhyolitic flows, the caldera-forming

106   eruption and ash-fall sheet, post-collapse rhyolitic flows, and resurgent domes (Christiansen and

107   Blank 1972; Christiansen 2001; Pierce et al. 2002; Pritchard and Larson 2012; Hurwitz and

108   Lowenstern 2014; Morgan et al. 2017). Small basaltic eruptions, minor compared to rhyolitic

109   material, occur throughout the cycle outside of the caldera boundaries. These cycles are

110   complete when basalt is able to erupt through the caldera floor, indicating the rhyolitic magma

111   has crystallized sufficiently to fracture and allow the denser basaltic melt to rise through it

112   (Hildreth et al. 1984). Since the formation of the Yellowstone caldera, post-collapse Plateau

113   Rhyolite flows fill much of it, but no post-collapse basaltic eruptive centers are found within the

114   caldera (Christiansen 2001; Hurwitz and Lowenstern 2014), supporting the idea that magma is

115   still present beneath the caldera.

116

117   **Geologic Setting of Study Area**

118   The study area, Seven Mile Hole (Fig 2), is located about 9 km east of the Lower Falls of

119   the Yellowstone River, between the Grand Canyon of the Yellowstone River and Washburn Hot

120   Springs, just south of Mt. Washburn. Exposed bedrock is dominated by several flows of the

121   Eastern Upper Basin Member, primarily the Tuff of Sulphur Creek and Canyon Flow

122   (Christiansen 2001; Pritchard and Larson 2012). Units of the Eastern Upper Basin Member are

123   some of the oldest post-collapse flows, collectively erupting about 481 ± 8 ka, and are deposited

124   north of the Sour Creek Resurgent Dome (Christiansen 2001; Pritchard and Larson 2012;

125   Hurwitz and Lowenstern 2014). Based on age and stratigraphic relations, the Eastern Upper

126   Basin Member stratigraphy, from oldest to youngest, is the Tuff of Uncle Tom's Trail, the Tuff

127   of Sulphur Creek, the Canyon Flow, and the Dunraven Road Flow (Christiansen 2001; Pritchard

128   and Larson 2012). The only exposure of the Tuff of Uncle Tom's Trail is a small, heavily

129   hydrothermally altered pyroclastic flow that may be related to the Tuff of Sulphur Creek

130   (Christiansen 2001; Pritchard and Larson 2012). The Tuff of Sulphur Creek, a low-δ^{18}O (1.9‰

131   from quartz), high silica, ignimbrite with variable welding, makes up the walls of the Grand

132   Canyon of the Yellowstone River. It covers approximately 119 km^2 and, at its type locality, is

133   about 230 m thick (Pritchard and Larson 2012). The Tuff of Sulphur Creek is separated into

134   three sections, basal, stony interior, and upper portion. Broadly, the flow contains 5-15 vol%

135   anhedral, rounded, and often embayed quartz phenocrysts, 20-35 vol% subhedral to anhedral

136   sanidine phenocrysts, 5-10 vol% subhedral sodic plagioclase, with minor to trace

137   titanomagnetite, magnetite, ilmenite, zircon, and apatite (Larson et al. 2009; Pritchard and

138   Larson 2012). The basal layer is comprised of two ash layers with 10-20% phenocrysts, each

139   approximately 2 m thick, separated by a 1 cm thick layer of welded ash, pumice, and lithic glass

140   fragments (Pritchard and Larson 2012). The stony interior, by far the thickest section, has crude

141   columnar jointing with areas of increased phenocryst (20-35%) and lithic abundances (Pritchard

142   and Larson 2012). The seldom exposed upper portion can grade from the stony interior to a

143   glass-rhyolite breccia (Pritchard and Larson 2012).

144   Overlying the Tuff of Sulphur Creek is the Canyon Flow, which is also divided into three

145   sections, basal, interior, and a glassy upper portion (Christiansen 2001; Pritchard and Larson

146   2012). The basal portion is nearly impossible to discern from the upper portion of the Tuff of

147   Sulphur Creek, unless there is flow banding present (Pritchard and Larson 2012). The interior

148   portion is, generally, a devitrified, light gray rhyolite with pink to red bands (Pritchard and

149   Larson 2012). The upper portion is, in some locations, a highly vesiculated breccia up to 2 m

150   thick (Pritchard and Larson 2012). The intermediate volcanic rocks of the Eocene Absaroka

151   Supergroup and its associated Mt. Washburn eruptive center are exposed on the north side of the

152   study area (Christiansen 2001; Feeley 2002; Pritchard and Larson 2012).

153   The two glacial periods on the Yellowstone Plateau, the Bull Lake (about 160 to 130 ka)

154   and Pinedale glaciations (about 22 to 14 ka), left deposits, such as diamicton and erratics, in and

155   around the study area mantling the Grand Canyon of the Yellowstone River (Pierce 1979;

156   Christiansen 2001; Licciardi et al. 2001; Licciardi and Pierce 2008; Larson et al. 2009; Licciardi

157   and Pierce 2018). The presence of sinter and hydrothermally altered and cemented sediments

158   suggests that the area was not extensively eroded since the last glaciation; however, material was

159   likely removed, meaning the paleosurface and modern Canyon rim are likely not at the same

160   elevation (Larson et al. 2009). Additionally, the extra hydrostatic head exerted from the glaciers

161   may explain some fluid inclusion homogenization temperatures with ranges that are higher than

162   the theoretical boiling-point curve suggests for the modern canyon rim elevation (Fournier 1989;

163   Christiansen 2001).

164

165   **Hydrothermal system at Yellowstone**

166   There are more than 10,000 surficial thermal features associated with the Yellowstone

167   caldera (Fig 1) with four distinct types of fluids; gas, alkaline-chloride fluids, acid-sulfate fluids,

168   and modern meteoric waters (Fournier 1989; Hurwitz and Lowenstern 2014). Modern meteoric

169   waters can accumulate on the surface or in shallow aquifers, and can be recognized by cooler

170   temperatures as well as elevated Ca and Mg concentrations. Data comprising local meteoric

171   waters was collected from snow and rain that fell in the mountains to the north, west, and east of

172   Yellowstone National Park (Kharaka et al. 2002). Stable isotope ratios indicate thermal fluids

173   are primarily derived from a meteoric source recharged during a cooler time, possibly during the

174   Bull Lake and/or Pinedale glaciations (Fournier 1989; Hurwitz and Lowenstern 2014).

175   Alkaline-chloride fluids have a neutral to slightly alkaline pH with elevated Cl^-, mostly

176   balanced by Na^+ with other alkali and alkaline earth elements balancing the remaining charge

177   (Hurwitz and Lowenstern 2014). These fluids discharge at topographic lows, mainly in the

178   western portion of the caldera (Fig 1) where, typically, they form clear hot springs and build

179   mounds of siliceous sinter (Fournier 1989; Hurwitz and Lowenstern 2014). Provided alkaline-

180   chloride fluids do not boil significantly as they rise, CO_2 and H_2S tend to be dissolved in them.

181   Boiling of an alkaline-chloride fluid could give rise to acid-sulfate fluids (Fournier 1989;

182   Hurwitz and Lowenstern 2014). Boiling liberates volatiles like H_2O, CO_2 and H_2S to the vapor

183   phase, concentrating less volatile constituents in the residual liquid. As the vapor phase rises, it

184   may condense into shallow, cold, dilute meteoric water where the pH is driven down from the

185   dissolution of CO_2 and H_2S.

$$CO_2 + H_2O \rightarrow H_2CO_3 \rightarrow HCO_3^- + H^+ \tag{1}$$

$$H_2S + minor\ O_2 \rightarrow H_2SO_4 \tag{2}$$
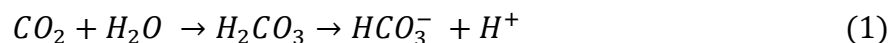
186   Equations 1 and 2 (Hedenquist and Arribas 2022) show CO_2 gas reacting with water to produce

187   H_2CO_3 before dissociating to HCO_3^- and H^+ and the oxidation of H_2S in a steam-heated

188   environment. The oxidation of H_2S can produce native sulfur and/or H_2SO_4 as well as

189   thiosulfate species, which can disproportionate to produce more acid (Xu et al. 1998; Hurwitz

190   and Lowenstern 2014). This sulfur oxidation path leads to the generation of an acid-sulfate fluid

191   where pH is typically between 1 and 5 with elevated sulfate concentrations (Hurwitz and

192   Lowenstern 2014). These fluids discharge mainly at local topographic highs in larger thermal

193   basins and tend to form depressions from acid-leaching of the host rock. Acid-sulfate fluids tend

194   to have significant dissolved silica, like alkaline-chloride fluids, but the low pH slows

195   deprotonation of silicic acid and nucleation of opal-A spheres (Iler 1979; Schintele et al. 2007).

196   Acid-sulfate fluids are discharged by a variety of features such as turbid hot springs with little

197   liquid discharge, mud pots, and fumaroles. (Fournier 1989). Gases discharged at fumaroles are

198   primarily water vapor, 90% to 99%, with CO_2 and H_2S making up the largest proportion of the

199   remaining constituents (Hurwitz and Lowenstern 2014).

200   Mixing of the fluid types, interaction with extra-caldera fluids, and/or interaction with

201   extra-caldera rocks produce hybrid fluids (Fournier 1989; Hurwitz and Lowenstern 2014). For

202   instance, Mammoth Hot Springs fluids, compared to alkaline-chloride fluids, have elevated Ca,

203   Mg, HCO_3^-, and SO_4^{2-} (Fournier 1989; Hurwitz and Lowenstern 2014), where Ca and HCO_3^- are

204   likely elevated due to alkaline-chloride fluids interacting with carbonate sedimentary rocks, e.g.,

205   the Mississippian Madison Limestone (Rye and Truesdell 2007). At Washburn Hot Springs,

206   acid-sulfate fluids likely interact with an organic-rich shale at depth liberating methane, ethane,

207   and ammonia, through distillation (Fournier 1989; Holloway et al. 2011; Hurwitz and

208   Lowenstern 2014).

209

210   **SAMPLING, METHODS, AND ANALYSES**

211   A sampling permit was issued by the National Park Service for three summers. Each

212   sample was located using a handheld Garmin GPSMAP 64 GPS unit. A total of 254 feldspars

213   and 31 sulfate mineral analyses were conducted using EMPA-WDS (electron microprobe

214   analysis with wave dispersive spectroscopy). The analyses were conducted in the Peter Hooper

215   GeoAnalytical Laboratory at Washington State University. The analyzed feldspar and sulfate

216   minerals come from eight and four different samples collected on Ridge 7741 and the South Fork

217   of Sulphur Creek, respectively (Fig 2). Discrete mineral analysis for major and trace element

218   concentrations were collected using a JEOL 8500F field emission electron microprobe with

219   diffracting crystals of TAP, PETJ, LIFH, a spot size of 5 microns, and 15 keV accelerating

220   voltage. Two analytical runs were conducted with the previous settings but with a beam current

221   of 15 nA and 20 nA.

222   Whole-rock XRF (x-ray fluorescence) and ICP-MS (inductively coupled plasma mass

223   spectrometry) data were measured on 81 samples representing various alteration styles and

224   intensity, veins, and siliceous sinter using methods in the Peter Hooper GeoAnalytical

225   Laboratory at Washington State University (Johnson et al. 1999). Whole-rock XRD (x-ray

226   powder diffraction) analysis was conducted at the Washington State University In Situ Reactive

227   Surface Analysis Center on a Rigaku Miniflex 600. Operating conditions were 15 mA and 40

228   kV using a CuKα ($\lambda\alpha1$ = 1.541) operated at with a 5 degree Soller collimator and

229   monochromator with a SC-70 detector. Whole-rock powder patterns were collected from 2° to

230   70° 2θ with 0.100 step increments at 8° per minute. Whole-rock powders were not treated prior

231   to analysis.

232   The mean whole-rock Ba concentration of the Tuff of Sulphur Creek is 932.08 (130.18)

233   ppm (Pritchard and Larson 2012). Ba is largely contained within sanidine phenocrysts and lesser

234   amounts in plagioclase and relatively minor amounts in the volcanic glass (Pritchard and Larson

235   2012). Data collected in this study largely overlaps with their data, but with a larger spread

236   because samples were not limited to unaltered rocks.

237   Feldspar analyses, data in Supplemental Table 4, plotted on a ternary diagram (Fig. 3)

238   indicate multiple primary feldspar compositions (sanidine, anorthoclase, oligoclase, andesine)

239   and adularia as a secondary feldspar. Figure 3 shows feldspar analyses that are separated into

240   their mode of occurrence, unaltered phenocrysts (Pritchard and Larson 2012), phenocryst, altered

241   phenocryst, devitrification products, and secondary. Phenocryst is a grain with minimal

242   replacement, altered phenocryst refers to grains where analysis was focused on the replaced

243   portions of the phenocryst, devitrification products are euhedral to subhedral feldspar crystals

244   found in vugs, and secondary feldspars are those found in veins. The data largely cluster in three

245   groups. The cluster around the orthoclase end member are secondary adularia and the other

246   clusters follow naming conventions displayed. Figure 4 shows feldspar Ba concentrations

247   plotted against orthoclase concentrations, separated in the same manner as Figure 3. Sanidine

248   phenocrysts fall between $Or_{34.84 - 61.00}$ with 0.00 to 1.95, mean 0.80 (0.75) wt% BaO. These

249   values agree with mean unaltered sanidine chemistry, $Or_{48.1}$ $Ab_{47.85}$ $An_{3.98}$ and 1.60 wt% BaO

250   (Pritchard and Larson 2012). Variations may arise because sanidine phenocrysts are chemically

251   zoned, as shown in Figure 5, where the lighter bands indicate greater concentrations of Ba.

252   Plagioclase grains have formulas ranging from $Or_{7.28 - 11.93}$ $Ab_{65.51 - 70.25}An_{19.66 - 26.22}$ with 0.19 to

253   0.42, mean 0.26 (0.06) wt% BaO. Only a few oligoclase samples came from veins; it is

254   unknown if those grains are primary or secondary. Adularia is primarily found in or near veins

255   where it replaces sanidine phenocrysts along fractures and/or crystal margins as well as growing

256   in open spaces. Adularia have $Or_{95.03 - 99.82}$ with 0.00 to 1.48, mean 0.46 (0.23) wt% BaO,

257   similar to sanidine, but typically with lower Ba concentrations.

258   Sulfate analyses come from alunite supergroup minerals (ASM) and two barite grains.

259   The barite grains were found in a silica-sulfide vein from the South Fork of Sulphur Creek as

260   fractured, anhedral crystals. ASM are found replacing groundmass as well as potassium

261   feldspars. These sulfate mineral formulas lie in the range $(K_{(0.75 - 0.91)}Ba_{(0.01 - 0.12)}Na_{(0 - 0.07)}Ca_{(0-}$

262    $_{0.01)}\square_{(0.01 - 0.12)})(Al_{(2.32-2.99)}Fe_{(0-0.67)}Mg_{(0-0.01)})(SO_4)_2(OH)_6$. Grain analyses range from 0.13 to 1.66,

263   mean 1.12 (0.37) wt% BaO. All ASM analyses required correction when calculating mineral

264   formulas, which will be discussed later.

265

Hydrothermal Mineralogy and Alteration Associations

267   The rocks in the study area have been altered by both acid-sulfate and alkaline-chloride

268   fluids, both of which are actively discharging in the area. The overall color of the weakly altered

269   Tuff of Sulphur Creek ranges from a dense black to purple, with medium gray groundmass with

270   lithophysae and spherulites (Larson et al. 2009) filled or partially filled with some combination

271   of silica, sulfides, and kaolinite/illite. More pervasive alteration can leave the unit yellow-white

272   or cream colored. A broken siliceous sinter field, now a fumarole field, is found between the

273   South Fork of Sulphur Creek and the modern rim of the Grand Canyon of the Yellowstone River

274   (Fig. 2) which indicates either alkaline-chloride fluids discharged at that elevation after the

275   Pinedale glaciation or there was insufficient glacial erosion to remove it. Currently, alkaline-

276   chloride fluids primarily discharge around 2300 m or lower. Acid-sulfate fluids discharge in the

277   South Fork of Sulphur Creek, a little less than 300 m north of the brecciated siliceous sinter field.

278   Neutral pH springs are found in Sulphur Creek just downstream of a small unnamed cascade;

279   fluids emanating from springs here, unofficially named "Cloudy Spring" (Fig 2), cause Sulphur

280   Creek to be cloudy.

281   Hydrothermal alteration can be separated based on location; Ridge 7741 and the South

282   Fork of Sulphur Creek are prominent zones altered by alkaline-chloride and acid-sulfate fluids,

283   respectively (Larson et al. 2009; Pritchard and Larson 2012). The red lines on Figure 2 are

284   resistant silicic cores of quartz, chalcedony, or opaline silica locally surrounded by illite + quartz

285   ± hydrothermal feldspar or kaolinite + opal/quartz ± ASM, depending on elevation. Vein

286   mineral assemblages at Ridge 7741 are characterized by quartz + adularia (less commonly

287   buddingtonite and hyalophane) ± ASM with a distal illite + quartz halo. In some areas near

288   veins, whole-rock XRD diffractograms suggest the presence of muscovite, possibly ordered

289   illite, potentially representing deeper alteration (John et al. 2010). Shallow alteration is

290   dominated by kaolinite with varying amounts of opal and ASM. Upper portions of upwelling

291   zones tend to have small halos of dickite ± ASM, usually with some amount of opaline silica.

292   Acid-sulfate alteration in the South Fork of Sulphur Creek is noted by bleached valley

293   walls with streaks of hematite-red and by silica ± sulfide veins and veinlets. The valley gets

294   deeper and the walls steeper as the South Fork of Sulphur Creek approaches its confluence with

295   Sulphur Creek. Approximately 12 to 24 m below the top of the valley are bodies of residual

296   quartz in close association with alunite-rich zones, however, alunite zones are not limited to a

297   certain depth. Wall rock in the area is replaced by kaolinite ± ASM ±opal. Veins and veinlets

298   cut the streambed and valley walls, getting progressively wider with more obvious brecciation

299   before thinning again closer to the confluence. These veins are composed of silica (typically

300   opaline but occasionally with fine grained quartz), sulfide (pyrite, marcasite, and trace galena,

301   sphalerite), ASM (alunite, walthierite, huangite, rostite) with lesser native sulfur and uncommon

302   barite. Breccia clasts are frequently altered to kaolinite + silica ± pyrite/marcasite. Nodules,

303   likely lithophysae, in the area are also filled or partially filled by silica ± sulfides ± native sulfur.,

304   usually with some amount of kaolinite.

305   Vertically, there are two broad alteration associations noted in the Grand Canyon walls,

306   quartz/opal + kaolinite and illite + quartz, noted in the upper canyon walls and nearer to the

307   Yellowstone River, respectively. Opal found deeper in the canyon appears to cross-cut veins

308   suggesting hydrothermal overprinting, perhaps developed as the canyon incised (Larson et al.

309   2009). Quartz/opal + kaolinite is most prominent in a zone from the modern rim of the Grand

310   Canyon of the Yellowstone River to approximately 75 - 100 m into the canyon where illite +

311   quartz becomes the dominant assemblage. Locally, there may be dickite or rarely nacrite and/or

312   alunite with trace barite. The kaolinite-illite transition may represent prolonged stability in the

313   water table, where distinct chemical zonation may have developed from differences in the

314   activity of K^+, pH, and/or temperature (Meyers and Hemley 1957; Inoue 1995; John et al. 2018).

315

316   **Paragenesis**

317   Hydrothermal mineral paragenesis in Seven Mile Hole varies depending on location.

318   However, a reasonable paragenesis can be clarified if it is assumed that the rocks first

319   experienced alkaline-chloride alteration followed by acid-sulfate alteration. This broad

320   assumption is based on the brecciated and extinct siliceous sinter field, a product of alkaline-

321   chloride fluids, at the modern Grand Canyon rim elevation that is now a fumarole field. A

322   similar transition was noted on the Mirror Plateau, where old siliceous sinter indicates this

323   current acid-sulfate hydrothermal area was once dominated by alkaline-chloride fluids that

324   discharged on the surface (Fournier 1989). In Seven Mile Hole, a string of siliceous sinter fields

325   leading to the Yellowstone River appear to indicate the progression of the upwelling zone(s) as

326   the water table lowered. As a consequence of lowering the water table, the steam-heated portion

327   of the system expanded and allowed for acid-sulfate fluids to discharge at the modern surface.

328   Figure 6 indicates the paragenesis for the system. Some minerals, like opal and kaolinite, are

329   produced throughout the life of the system (Larson et al. 2009) because these are common

330   minerals in steam-heated portions of hydrothermal systems (John et al. 2010). However, Figure

331   6 does not reflect this pattern in order to examine the overall progression of hydrothermal

332   alteration.

333   In the deepest portions of the system, exposed at and around Ridge 7741 (Fig 2),

334   hydrothermal alteration is dominated by illite + quartz and veins are mainly quartz +

335   hydrothermal feldspars, primarily adularia with rare hyalophane and buddingtonite. Vein

336   paragenesis starts with adularia, noted as small crystals projecting inward from vein walls and as

337   replacement of sanidine phenocrysts. Sanidine phenocrysts in a vein may be replaced by

338   adularia along crystal margins, fractures, and/or as irregular masses throughout the grain,

339   potentially taking advantage of cleavage planes. Figure 7A shows a sanidine phenocryst with

340   partial replacement by adularia along curving fracture planes and as irregular masses. Quartz

341   precipitated throughout the life of the veins.

342   Approximately 25 m below the top of the ridge is a quartz + pyrite/marcasite + illite

343 breccia that poorly outcrops on the southwestern side. Breccia clasts were altered to illite before

344 being silicified, indicating brecciation occurred after illite + quartz alteration. Pyrite and

345 botryoidal marcasite are mainly found in the quartz-rich matrix, but some grains are associated

346 with the margins of clasts. Minor native sulfur is present as scattered millimeter-sized anhedral

347 masses closely associated with marcasite and as submillimeter grains in clay pockets suggesting

348 a similar or slightly later paragenetic relation as marcasite and pyrite.

349   Later acid-sulfate fluids altered adularia and remaining sanidine to kaolinite and ASM

350 with minor montmorillonite. ASM appear paragenetically older than the phyllosilicates. Pyrite

351 and/or marcasite, appears to have occurred around the same time as alunite and phyllosilicate

352 formation, but more precise timing is unknown. Elongated, radiating, and blocky pyrite anneal

353 brecciated botryoidal and laminated marcasite as well as replace it. Previous studies found

354 galena and sphalerite via XRD, but only possible sphalerite was noted via EPMA. The small

355 potential sphalerite grains were found near the grain boundary between marcasite and pyrite,

356 suggesting it is younger than marcasite and about the same age as pyrite. Only a few small

357 anhedral barite grains were found; these grains are paragenetically late, found near the center of

358 quartz veins.

359   In more shallow alteration, similar paragenetic stages are followed, except kaolinite is

360 stable instead of illite, adularia is not present, and silica is found as druzy quartz, tridymite,

361 and/or opal. Shallow distal alteration is mainly noted as kaolinite replacing groundmass and

362 phenocrysts with or without silica. Vugs are typically coated with millimeter-sized druzy quartz

363 and partially filled with kaolinite ± ASM, commonly stained with iron oxides. Near upwelling

364 centers, ASM become more common. Shallow expressions of upwelling centers have halos of

365   dickite + opal/tridymite ± alunite supergroup minerals. Slightly deeper, hotter portions of

366   upwelling centers have the same assemblages except dickite may be rarely associated with

367   pyrophyllite.

368

369   **DISCUSSION**

370   **Problems with alunite formula calculations**

371   Alunite supergroup minerals follow the general formula $DG_3(TX_4)_2X'_6$, where D may

372   contain K, Na, Ba, Ca, or be vacant; G may contain Al, Fe3+, Mg; T may contain S, P, As; X/X'

373   may contain O, OH, F, H_2O; a more complete list of substitutions can be found in Bayliss et al.

374   (2010). Electron backscattter images (Fig 7B-E) indicate that ASM are solid-solution mixtures

375   with compositional zonation, which is not uncommon (Bayliss et al. 2010). However, if

376   replacement of potassium feldspars by ASM occurred before equilibrium between alunite and the

377   silicates in the host rock was reached, $KSO_4(aq)$, $AlSO_4(aq)$ and complex aluminum hydroxides

378   can form (Hemley et al. 1969). Under experimental conditions, boehmite was produced,

379   however, diaspore is the characteristic phase in natural conditions (Hemley et al. 1969). Figure

380   7D shows how intimately ASM (slightly lighter gray) and kaolinite (darkest) may be associated.

381   Without correction, both stoichiometry and electrostatic charge for 6 atoms per formula

382   unit are out of balance from excess Al and S. Since alunite can have a vacancy in the D site,

383   focus was placed on the amount of S present. However, even using idealized Al:S, the

384   stoichiometric imbalance persisted. To account for too much Al, end members for Na, K, Ba,

385   and Ca (natroalunite, alunite, walthierite, and huangite, respectively) were calculated. Simple

386   subtraction showed there was still excess S and Al. Chemically, this could constitute rostite

387   ($Al(SO_4)OH·5H_2O$) or jurbanite ($Al(SO_4)OH·5H_2O$). Whole-rock XRD diffractograms indicate

388   jurbanite is a possibility and previous studies found rostite, but more precise chemical and crystal

389   structure data are needed to further identify the mineral species. Regardless of which mineral is

390   truly present, each have equal proportions of Al and S. This method indicates the grains possibly

391   have a fairly large proportion of rostite/jurbanite and alunite with lesser walthierite, minor

392   natroalunite and trace huangite. Supplemental Table 3 shows the idealized formulas and amount

393   of $AlSO_4(OH) \cdot 5H2O$, calculated as rostite. It should be noted that after this correction, most

394   analyses still have an excess of Al which may indicate that there is a portion of some aluminum

395   oxide or hydroxide not accounted for and not identified in XRD diffractograms, potentially

396   indicating disequilibrium between host rock silicate minerals and ASM during alteration or a

397   physical mixture not seen at the scale of analysis.

398   This treatment seems to indicate each analysis has roughly 40 to 70% rostite. One

399   possible downside is that the method may work to minimize vacancies in the D site, however,

400   there are still vacancies in the formulas when normalized to 6 atoms per formula unit.

401   Regardless, Supplemental Table 3 indicates ASM are mostly Ba-bearing alunite with lower

402   concentrations of Na and occasionally Ca. Most of the Ba-bearing alunite grains have a G-site

403   filled with Al and minor Mg, however, there are two analyses with elevated Fe. These analyses

404   are from alunite grains with jarosite rims (Fig 7E), where paragenetically older alunite has an

405   overgrowth of jarosite, the brighter rim, from a later acidic event.

406

407   **Barium in a dynamic hydrothermal system**

408   When examined separately, Ridge 7741 and the South Fork of Sulphur Creek allow for a

409   model of the hydrothermal evolution for Seven Mile Hole to be constructed. Alkaline-chloride

410   fluids rose along a presumed structural channel forming an erosion resistant silicified ridge,

411   Ridge 7741 (Fig 2) (Larson et al. 2009). Continued upflow produced illite + quartz ±

412   hydrothermal feldspar, primarily adularia. For adularia to be stable over illite or muscovite,

413   aK^+/aH^+ must be slightly elevated, likely due, in part, to a near neutral pH (Meyer and Hemley

414   1957; Inoue 1995; White and Hedenquist 1995). Farther from the main upwelling portions and

415   veins, the presence of illite without adularia indicates either a lower aK^+/aH^+, a general decrease

416   in temperature, or some combination, provided pressure remains the same (Fig 8).

417   Veins associated with Ridge 7741 are primarily quartz with lesser clay, adularia, and

418   pyrite. In the veins, entrained sanidine phenocrysts may be replaced by adularia or adularia may

419   crystallize from the fluid, indicating an alkaline-chloride fluid composition. Sanidine

420   phenocrysts from the Tuff of Sulphur Creek have an mean formula of

421     $(K_{.49}Na_{.43}Ca_{.03}Ba_{.03})AlSi_3O_8$ with 0.11 to 2.13 wt% BaO (Pritchard and Larson 2012). Mean

422   adularia formula range as $(K_{.84-.99}Na_{0-.06}Ba_{0-.03})AlSi_3O_8$, where Ba ranges from 0.00 to 1.48 wt%

423   BaO. Analyses on adularia that are not the product of phenocryst replacement tend to have less

424   BaO (0.02 to 0.88 wt%) than adularia as a replacement product of sanidine phenocrysts (0.00 to

425   1.48 wt%), but both styles have similar mean values (0.45 and 0.46 wt% BaO, respectively).

426   Replacement acts to liberate constituents and drive crystal chemistry toward $KAlSi_3O_8$.

427   Hyalophane $((K, Ba)AlSi_3O_8)$ was only noted in XRD diffractograms, potentially indicating it is

428   a minor or intermediate phase. If it is an intermediate or minor product of hydrothermal

429   alteration, hyalophane may point to the preferential leaching of Ca and Na over Ba and K from a

430   sanidine phenocryst.

431   In contrast to the alkaline-chloride assemblage at Ridge 7741, shallow hydrothermal

432   alteration noted in the South Fork of Sulphur Creek is mostly lacking in alkaline-chloride

433   mineral assemblages. The most common and widespread mineral assemblage in the area is

434   kaolinite + opaline silica/duzy quartz ± ASM ± pyrite/marcasite with barite disseminated in the

435   wall rock along the modern valley rim, and more rarely in the stream bed. Above approximately

436   2440 m, elongate bodies of dickite, quartz, and rare pyrophyllite and diaspore are associated with

437   the more widespread mineral assemblage (Fig 2). The presence of dickite and pyrophyllite

438   indicate higher temperatures than areas with just kaolinite, and may indicate upwelling zones

439   (John et al. 2010; Hedenquist and Arribas 2022). These mineral assemblages are typical of acid-

440   sulfate alteration in silicate rocks (Hemley and Jones 1964; Hemley et al. 1969). Remnants of

441   alkaline-chloride fluid interaction are still present as bodies of quartz + albite + illite + pyrite,

442   interpreted as propylitic alteration (John et al. 2010), as well as the broken siliceous sinter field

443   (Fig 2).

444   In this shallow acid-sulfate environment, Ba-bearing ASM replace sanidine phenocrysts

445   and adularia. ASM typically have similar to slightly elevated concentrations of Ba, relative to

446   adularia noted at Ridge 7741 (0.13 to 1.66 and 0.00 to 1.48 wt% BaO, respectively). Acid-

447   sulfate fluids, produced from shallow oxidation of H_2S (Stoffregen 1987; Fournier 1989), in

448   conjunction with feldspars in the Tuff of Sulphur Creek, provide all of the necessary ingredients

449   for the shallow acid assemblage, where, provided the Tuff of Sulphur Creek was previously

450   altered to mineral assemblages similar to Ridge 7741, illite is replaced by kaolinite and K-

451   feldspar may be replaced by ASM and quartz as follows.

$$3KAlSi_3O_8 + 6H^+ + 2SO_4^{2-} = KAl_3(SO_4)_2(OH)_6 + 2K^+ + 9SiO_2 \qquad (3)$$
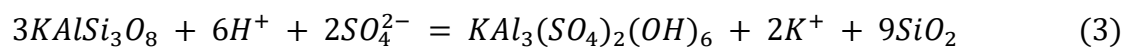
452   The reaction in equation 3 (Hemley et al. 1969) describes the consumption of H^+ and SO_4^{2-} while

453   liberating K^+ and SiO_2. Hydrogen and sulfate consumed in the reaction are produced from

454   dissociation of H_2SO_4 produced in equation 2 and disproportionation of $SO_2(g)$. Continued

455 exposure to low pH fluids replaced some alunite with kaolinite along irregular and ratty edges

456 (Fig 7D).

457 $$2KAl_3(SO_4)_2(OH)_6 + 3H_2O + 6SiO_2(aq) = 3Al_2(Si_2O_5)(OH)_4 + 2K^+ + 6H^+ + 4SO_4^{2-} \quad (4)$$
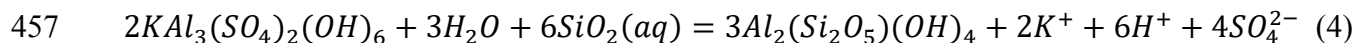
458 The reaction in equation 4 (Hemley et al. 1969) produces a lower pH fluid through the release of

459 hydrogen ions. At a sufficiently low pH, hydrolytic alteration can begin to leach even relatively

460 immobile components like Al^{3+}, leading to bodies of residual quartz (Hemley and Jones 1964;

461 Stoffregen 1987; Hedenquist and Arribas 2022), like those noted in the upper valley walls of the

462 South Fork of Sulphur Creek.

$$0.5Al_2(Si_2O_5)(OH)_4 + 3H^+ \rightarrow SiO_2 + 2.5H_2O + Al^{3+} \quad (5)$$
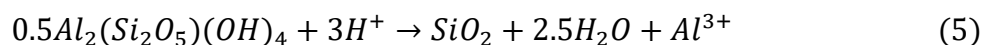
463 Equation 5 (Stoffregen 1987) indicates how kaolinite can be broken down to quartz and water

464 while liberating Al^{3+}. XRF and ICP-MS analyses indicate samples with greater concentrations of

465 silica commonly have lower concentrations of Ba and most other constituents (Supplemental

466 Tables 1 and 2).

467 Barite seems to be part of a late-stage event. There is one occurrence noted in the center

468 of a quartz veinlet in the South Fork of Sulphur Creek with scattered occurrences around the

469 valley rim and rare occurrences at the rim of the Grand Canyon of the Yellowstone River, noted

470 via XRD. Without noting more textural variations and paragenetic relations, it is difficult to say

471 if some or all barite in the system is part of a late-stage hypogene or supergene event. In either

472 case, it shows Ba can remain dissolved in the fluid, even at relatively shallow depths.

473 The Ba redistribution in the relatively shallow portions of the Seven Mile Hole system

474 can be compared to Ba mobility in clasts from explosion craters in Yellowstone Lake (Morgan et

475 al. 2009). Explosion breccia clasts are commonly silicified and sulfidized, with veinlets and

476 occasional calcite. Whole-rock analyses of clasts indicate Ba concentrations up to 1700 ppm

477   (Morgan et al. 2009). The modern altered lacustrine sediments from the Mary Bay crater (80 to

478   630 ppm Ba) (Morgan et al. 2009) appear have modest enrichment, similar to the Tuff of Sulphur

479   Creek. Morgan et al. (2009) suggest that the thermal fluids are not significant sources of Ba and

480   that Ba in the altered rock was sourced from the host rock. Mass-balance calculations of thermal

481   fluid influx into Yellowstone Lake show that the thermal fluids are not significant sources of Ba

482   (Balistrieri et al. 2007). This reinforces the idea that Ba in the thermal fluids is sourced from

483   host rock and is redistributed by that fluid. However, vents within Yellowstone Lake show a

484   correlation between higher Ba and CO_2 concentrations. The area is seismically active

485   (Christiansen 2001; Morgan et al. 2009). Seismicity could open pathways for deeper reservoir

486   fluids with higher concentrations of Ba and CO_2 to rise to near the surface (Fournier 1989;

487   Hurwitz and Lowenstern 2014). A release of deep reservoir fluids is possible due to the

488   proximity to the caldera ring-fault allowing greater permeability, but the modest change in Ba

489   concentration from altered and unaltered Tuff of Sulphur Creek indicates little addition of Ba to

490   the unit unless glacial erosion has removed the signature. Data from across the Yellowstone

491   hydrothermal system indicate, while the thermal areas may be transient, general fluid chemistry

492   remains fairly predictable but can be modified by boiling, mixing with shallow meteoric water,

493   and water-rock interactions (Fournier 1989; Hurwitz and Lowenstern 2014).

IMPLICATIONS

495   Recycling of hydrothermally altered magmatic materials appears to be a common event

496   associated with Yellowstone volcanism, as noted by stable isotopes. A hydrothermal system,

497   dominated by meteoric fluids, can lower the ^{18}O signature of a rock while liberating constituents,

498   such as Ba, from primary magmatic phases to sequester them into minerals that are more stable

499   at lower temperatures. When exposed to magmatic temperatures, hydrothermally altered

500   portions may preferentially melt, leading to trends noted not only in Yellowstone but also in the

501   North American Cordillera.

502   The past three volcanic cycles associated with the Yellowstone hotspot produced low

503     $\delta^{18}O$ rhyolites after the eruption of a major ash-fall sheet (Bindeman and Valley 2001). There

504   are two competing hypotheses for the formation of low $\delta^{18}O$ magmas at Yellowstone, the

505   introduction of meteoric water to the magma chamber or assimilation and partial melting of

506   hydrothermally altered material; the latter hypothesis is more widely accepted (Bindeman and

507   Valley 2001; Pritchard and Larson 2012). Hot, circulating meteoric water above and around the

508   Yellowstone magma chamber will hydrothermally alter the country rock and deplete the ^{18}O

509   signature of that rock (Christiansen 2001; Pritchard and Larson 2012; Hurwitz and Lowenstern

510   2014). Caldera collapse brings hydrothermally altered rock in the caldera lid closer to hotter

511   material deeper in the magma chamber, where portions of the hydrothermal assemblages can

512   preferentially melt to create a magma with a depleted oxygen isotopic signature, relative to

513   typical magmatic values, 6 to 10‰ (Sharp 2017). The Tuff of Sulphur Creek is a low $\delta^{18}O$

514   unit,1.9‰ from quartz, with elevated Ba concentrations, and is one of the oldest post-collapse

515   units in the 0.639 Ma Yellowstone caldera (Hildreth et al. 1984; Christiansen 2001; Pritchard and

516   Larson 2012).

517   The current study indicates that hydrothermal alteration will liberate constituents like Ba

518   from primary magmatic phases to phases that are more stable at lower temperatures, such as

519   barite and ASM. Integrating the model of partial melting of hydrothermally altered material with

520   the observation that epithermal alteration replaces high temperature minerals with lower

521   temperature minerals may explain why Cenozoic North American Cordillera rhyolite mean Ba

522   concentrations are elevated relative to mean upper crustal concentrations, about 630 ppm

523   (Rudnick and Gao 2003). Faulting due to Basin and Range extension in the western United

524   States thinned the crust and created NNW-striking normal faults that provided planes of

525   weakness for some Yellowstone volcanic vents (Christiansen 2001). Provided magma can

526   follow these faults, it is reasonable to imagine meteoric water also following these faults, only to

527   be heated up at depth and rise buoyantly to generate epithermal-style hydrothermal alteration.

528   Preferential melting and recycling of the altered rock may produce Cenozoic rhyolites with

529   elevated Ba. While some of the Ba may be sourced from aqueous fluids exsolving from rising

530   basaltic melts, isotopic studies of barium are needed to better understand the source mechanisms

531   behind the elevated barium concentrations in the Cenozoic rhyolites.

532

544   **REFERENCES**

545   Bachmann, O., Deering, C.D., Lipman, P.W., and Plummer, C. (2014) Building zoned

546   ignimbrites by recycling silicic cumulates: insight from the 1,000 km^3 Carpenter Ridge

547   Tuff, CO, Contributions to Mineralogy Petrology, 167(6), p. 1 – 13. doi: 10.1007/s00410-

548   014-1025-3.

549   Balistrieri, L.S., Shanks, W.C. III, Cuhel, R.L., Aguilar, C. and Klump, J.V. (2007) The

550   influence of sublacustrine hydrothermal vent fluids on the geochemistry of Yellowstone

551   Lake. In L.A. Morgan Ed., Integrated Geoscience Studies in the Greater Yellowstone

552   Area -Volcanic, Tectonic, and Hydrothermal Processes in the Yellowstone Geoecosystem

553   p. 173-199 USGS Professional Paper 1717.

554   Bayliss, P., Kolitsch, U., Nickel, E.H., and Pring, A. (2010) Alunite supergroup: recommended

555   nomenclature. Mineralogical Magazine, 74, 919-927. doi:

556   10.1180/minmag.2010.074.5.919.

557   Bindeman, I.N., and Valley, J.W. (2001) Low-δ^{18}O rhyolites from Yellowstone: magmatic

558   evolution based on analyses of zircons and individual phenocrysts. Journal of Petrology,

559   42, 1491-1517. doi: 10.1093/petrology/42.8.1491

560   Brueseke, M.E., Callicoat, J.S., Hames, W., and Larson, P.B. (2014) Mid-Miocene rhyolite

561   volcanism in northeastern Nevada: the Jarbidge rhyolite and its relationship to the

562   Cenozoic evolution of the northern Great Basin (USA): Geological Society of America

563   Bulletin, v.126, p. 1047-1067. doi: 10.1130/B30736.1.

564   Christiansen, E.H. and McCurry, M. (2008) Contrasting origins of Cenozoic silicic volcanic

565   rocks from the western Cordillera of the United States. Bullient of Volcanology, 70, 251-

566   267. doi: 10.1007/s00445-007-0138-1.

567   Christiansen, R.L. (2001) The Quaternary and Pliocene Yellowstone Plateau volcanic field of

568   Wyoming, Idaho, and Montana. USGS Professional Paper 729-G Washington D.C., 156

569   p. doi: 10.3133/pp729G.

570   Christiansen, R.L. and Blank, H.R. Jr (1972) Volcanic stratigraphy of the Quaternary rhyolite

571   plateau in Yellowstone National Park. USGS Professional Paper 729-B, Washington

572   D.C., 17 pp. doi: 10.3133/pp729B.Emmons, W.H. and Larsen E.S. (1923) Geology and

573   ore deposits of the Creede district, Colorado. USGS Bulletin 718, Washington D.C., 198

574   pp. doi:10.3133/b718.

575   Fournier, R.O. (1989) Geochemistry and dynamics of the Yellowstone National Park

576   hydrothermal system. Annual Review of Earth and Planetary Sciences, 17, 13-53. doi:

577   10.1146/annurev.ea.17.050189.000305.

578   Hildreth, W., Christiansen, R.L., and O'Neil, J.R. (1984) Catastrophic isotopic modification of

579   rhyolitic magma at times of caldera subsidence, Yellowstone Plateau volcanic field.

580   Journal of Geophysical Research: Solid Earth, 89, 8339-8369. doi:

581   10.1029/JB089iB10p08339.

582   Holloway, J.M., Nordstrom, D.K., Böhlke, J.K., McCleskey, R.B., and Ball, J.W. (2011)

583   Ammonium in thermal waters of Yellowstone National Park: processes affecting

584   speciation and isotope fractionation. Geochimica et Cosmochimica Acta, 75, 4611-4636.

585   doi: 10.1016/j.gca.2011.05.036.

586   Hurwitz, S., and Lowenstern, J.B. (2014) Dynamics of the Yellowstone hydrothermal system.

587   Reviews of Geophysics, 51, 375–411, doi:10.1002/2014RG000452

588 Inoue, A. (1995) Formation of clay minerals in hydrothermal environments. In B. Velde, Ed.,

589   Origin and Mineralogy of Clays: Clays and the Environment. p. 268-329 Springer Berlin,

590   Heidelberg. doi: 10.1007/978-3-662-12648-6_7.

591 John D.A. (2001) Miocene and early Pliocene epithermal gold-silver deposits in the northern

592   Great Basin, Western United States: characteristics, distribution, and relationship to

593   magmatism. Economic Geology, 96, 1827-1853.

594   https://doi.org/10.2113/gsecongeo.96.8.1827

595 John, D.A., Vikre, P.G., du Bray, E.A., Blakely, R.J., Fey, D.L., Rockwell, B.W., Mauk, J.L.,

596   Anderson, E.D., and Graybeal, F.T. (2010) Descriptive models for epithermal gold-silver

597   deposits. USGS Scientific Investigations Report 2010-5070-Q, 247 pp.

598   doi:10.3133/sir20105070Q.

599 Johnson, D.M., Hooper, P.R., and Conrey, R.M. (1999) XRF analysis of rocks and minerals for

600   major and trace elements on a single low dilution Li-tetraborate fused bead. Advances in

601   X-Ray Analysis, 41, 843-867.

602 Kharaka, Y.K., Thordsen, J.J., and White, L.D. (2002) Isotope and chemical compositions of

603   meteoric and thermal waters and snow from the greater Yellowstone National Park

604   Region. USGS Open File Report 02-194, 75 pp. doi: 10.3133/ofr02194.

605 Larson, P.B., Phillips, A., John, D., Cosca, M., Pritchard, C., Andersen, A., and Manion, J.

606   (2009) A preliminary study of older hot spring alteration in Sevenmile Hole, Grand

607   Canyon of the Yellowstone River, Yellowstone Caldera, Wyoming. Journal of

608   Volcanology and Geothermal Research, 188, 225-236. doi:

609   10.1016/j.jvolgeores.2009.07.017.

610   Lehnert, K., Profeta, L., Ramdeen S., Sweets, H., Ji, P., Figueroa, J.D., Cao, S., Robinson, S.,

611   Block, K., Grossberg, M., Ustunisik, G., Nielsen, R., and Walker, D. (2021) Earthchem

612   Portal (Online). Available: http://portal.earthchem.org/ (accessed Feb 2, 2023). Lamont-

613   Doherty Earth Observatory, New York, New York.

614   Licciardi, J.M., Clark, P.U., Brook, E.J., Pierce, K.L., Kurz, M.D., Elmore, D., and Sharma, P.

615   (2001) Cosmogenic ^{3}He and ^{10}Be chronologies of the late Pinedale northern Yellowstone

616   ice cap, Montana, USA. Geology, 29, 1095-1098. doi: 10.1130/0091-

617   7613(2001)029<1095:CHABCO>2.0.CO;2.

618   Licciardi, J.M. and Pierce, K.L. (2008) Cosmogenic exposure-age chronologies of Pinedale and

619   Bull Lake glaciations in greater Yellowstone and the Teton Range, USA. Quaternary

620   Science Reviews, 27, 814-831. doi: 10.1016/j.quascirev.2007.12.005.

621   ——— (2018) History and dynamics of the greater Yellowstone Glacial System during the last

622   two glaciations. Quaternary Science Reviews, 200, 1-33. doi:

623   10.1016/j.quascirev.2018.08.027.

624   Long, S.P. (2019) Geometry and magnitude of extension in the Basin and Range Province

625   (39°N), Utah, Nevada, and California, USA: constraints from a province-scale cross

626   section. Geological Society of America Bulletin, 131, 99-119. DOI: 10.1130/B31974.1.

627   Long, S.P., Heizler, M.T., Thomson, S., Reiners, P.W., and Fryxell, J.E. (2018) Rapid Oligocene

628   to early Miocene extension along the Grant Range detachment system, Nevada, USA:

629   Insights from multipart cooling histories of footwall rocks. Tectonics, 37,4752–4779.

630   DOI: 10.1029/2018TC005073.

631   Love, J.D. and Good, J.M. (1970) Hydrocarbons in thermal areas, northwestern Wyoming.

632   USGS Professional Paper 644-B, 23, pp. doi: 10.3133/pp644B.

633   Manion, J.L. (2010) Epithermal alteration in Tuff of Sulphur Creek, Yellowstone National Park,

634   Wyoming, 140 p. Masters thesis, Washington State University, Pullman.

635   Matthews, N.E., Vazquez, J.A. and Calvert, A.T. (2015) Age of the Lava Creek supereruption

636   and magma chamber assembly at Yellowstone based on ^{40}Ar/^{39}Ar and U-Pb dating of

637   sanidine and zircon crystals. Geochemistry, Geophysics, Geosystems, 16, 2508–2528.

638   doi:10.1002/2015GC005881.

639   Morgan, L.A., Shanks, W.C.P. III, and Pierce, K.L. (2009) Hydrothermal processes above the

640   Yellowstone magma chamber: Large hydrothermal systems and large hydrothermal

641   explosions. Geological Society of America Special Paper 459, 95 pp.

642   https://doi.org/10.1130/2009.2459(01).

643   Morgan, L.A., Shanks, W.C.P., Lowenstern, J.B., Farrell, J.M., and Robinson, J.E. (2017)

644   Geologic field-trip guide to the volcanic and hydrothermal landscape of the Yellowstone

645   Plateau. USGS Scientific Investigations Report 2017–5022–P, 100 pp.

646   https://doi.org/10.3133/sir20175022P.

647   Nan, X.Y., Yu, H.M., Rudnick, R.L., Gaschnig, R.M., Xu, J., Li, W.Y., Zhang, Q., Jin, Z.D., Li,

648   F.H., and Huang, F. (2018) Barium isotopic composition of the upper continental crust.

649   Geochimica et Cosmochimica Acta, 233, 33-49. doi: 10.1016/j.gca.2018.05.004.

650   Pierce, K.L. (1979) History and dynamics of glaciation in the northern Yellowstone National

651   Park area. USGS Professional Paper 729-F, 90 pp. doi: 10.3133/pp729F.

652   Pierce, K.L., Cannon, K.P., Meyer, G.A., Trebesch, M.J., and Watts, R.D. (2002) Post-glacial

653   inflation-deflation cycles, tilting, and faulting in the Yellowstone caldera based on

654   Yellowstone Lake shorelines. USGS Open File Report 2002-142, 30 pp. doi:

655   10.3133/ofr02142.

656   Phillips, A.R. (2010) An oxygen isotope, fluid inclusion, and mineralogy study of the ancient

657   hydrothermal alteration in the Grand Canyon of the Yellowstone River, Yellowstone

658   National Park, Wyoming, 97 p. Masters thesis, Washington State University, Pullman.

659   Pritchard, C.J., and Larson, P.B. (2012) Genesis of the post-caldera eastern Upper Basin Member

660   rhyolites, Yellowstone, WY: from volcanic stratigraphy, geochemistry, and radiogenic

661   isotope modeling. Contributions to Mineralogy and Petrology, 164, 205-228. doi:

662   10.1007/s00410-012-0733-9.

663   Rudnick, R.L. and Gao, S. (2003) Composition of the continental crust. In H.D. Holland and K.K

664   Turekian, Eds., Treatise on Geochemistry, 2nd ed., 3, 1-64. doi: 10.1016/B0-08-043751-

665   6/03016-4.

666   Rivera, T.A., Darata, R., Lippert, P.C., Jicha, B.R., and Schmitz, M.D. (2017) The duration of a

667   Yellowstone super-eruption cycle and implications for the age of the Olduvai subchron.

668   Earth and Planetary Science Letters, 479, p. 377-386. doi: 10.1016/j.epsl.2017.08.027.

669   Rye, R.O. and Truesdell, A.H. (2007) The question of recharge to the deep thermal reservoir

670   underlying the geysers and hot springs of Yellowstone National Park. In L.A. Morgan,

671   Ed., Integrated Geoscience Studies in the Greater Yellowstone Area – Volcanic,

672   Tectonic, and Hydrothermal Processes in the Yellowstone Geoecosystem: USGS

673   Professional Paper 1717, 239-270. doi: 10.3133/PP1717H.

674   Sharp, Z.D. (2017) Principles of stable isotope geochemistry, 2nd edition, 382 p. University of

675   New Mexico.

676   Smith, R.B., Jordan, M., Steinberger, B., Puskas, C.M., Farrell, J., Waite, G.P., Husen, S.,

677   Chang, W.L., and O'Connell, R. (2009) Geodynamics of the Yellowstone hotspot and

678   mantle plume: seismic and GPS imaging, kinematics, and mantle flow. Journal of

679   Volcanology and Geothermal Research, 188, 26-56. doi:

680   10.1016/j.jvolgeores.2009.08.020.

681   Stelten, M.E., Cooper, K.M., Vazquez, J.A., Calvert, A.T., and Glessner, J.G. (2015)

682   Mechanisms and timescales of generating eruptible rhyolitic magmas at Yellowstone

683   caldera from zircon and sanidine geochronology and geochemistry. Journal of Petrology,

684   56, 1607-1642. doi: 10.1093/petrology/egv047.

685   Stoffregen, R. (1987) Genesis of acid-sulfate alteration and Au-Cu-Ag mineralization at

686   Summitville, Colorado. Economic Geology, 82, 1575-1591. doi:

687   10.2113/gsecongeo.82.6.1575.

688   Swallow, E.J., Wilson, C.N.J., Charlier, B.L.A., and Gamble, J.A. (2019) The Huckleberry

689   Ridge Tuff, Yellowstone: evacuation of multiple magmatic systems in a complex

690   episodic eruption. Journal of Petrology, 60, 1371-1426. doi: 10.1093/petrology/egz034.

691   Till, C.B., Vazquez, J.A., Stelten, M.E., Shamloo, H.I., and Shaffer, J.S. (2019) Coexisting

692   discrete bodies of rhyolite and punctuated volcanism characterize Yellowstone's post-

693   Lava Creek Tuff caldera evolution. Geochemistry, Geophysics, Geosystems, 20, 3861–

694   3881. doi: 10.1029/2019GC008321.

695   Troch, J., Ellis, B.S., Harris, C., Ulmer, P., and Bachmann, O. (2018) The effect of prior

696   hydrothermal alteration on the melting behaviour during rhyolite formation in

697   Yellowstone, and its importance in the generation of low-δ^{18}O magmas. Earth and

698   Planetary Science Letters, 481, 338-349. doi: 10.1016/j.epsl.2017.10.039

699   Warr, L.N. (2021) IMA-CNMNC approved mineral symbols. Mineralogical Magazine, 85, 291-

700   320. doi: 10.1180/mgm.2021.43.

701   White, N.C. and Hedenquist, J.W. (1995) Epithermal gold deposits: styles, characteristics, and

702   exploration. Society of Economic Geologists Newsletter, p. 9-13. doi:

703   10.5382/SEGnews.1995-23.fea.

704   Xu, Y., Schoonen, M.A.A., Nordstrom, D.K., Cunningham, K.M., and Ball, J.W. (1998) Sulfur

705   geochemistry of hydrothermal water in Yellowstone National Park: I. the origin of

706   thiosulfate in hot spring waters. Geochimical et Cosmochimica Acta, 62, 3729 – 3743.

707   doi: 10.1016/S0016-7037(98)00269-5.

708   Captions for figures

709   Figure 1: Yellowstone National Park boundary with regional faults, 1st, 2nd, and 3rd cycle caldera

710   margins, Sour Creek and Mallard Lake resurgent domes, and thermal features, data from

711   Wyoming State Geological Survey GIS database (https://www.wsgs.wyo.gov/pubs-

712   maps/gis.aspx accessed Feb 16, 2022) and the Digital geologic-GIS map of the Yellowstone

713   National Park. Labeled thermal areas are MHS - Mammoth Hot Springs, WHS - Washburn Hot

714   Springs, LGB - Lower Geyser Basin, UGB - Upper Geyser Basin, SGB - Shoshone Geyser

715   Basin, SCTA – Spirea Creek Thermal Area.

716   Figure 2: Mineral assemblage map for Seven Mile Hole. The base map is a portion of the 1x1

717   degree Ashton E Wyoming topographic map

718   (https://rockyweb.usgs.gov/vdelivery/Datasets/Staged/Elev/Shape/ accessed Oct. 15, 2020).

719   Dataset is enhanced by data presented in Masters theses (Manion 2010; Phillips 2010). Each

720   color shows the various alteration assemblages and crossed areas are siliceous sinter fields.

721   MA5 zeolitic contains minerals from MA1 plus zeolite minerals. Red lines with an orange

722   outline (MA4) are silicified ridges and fingers. Most abbreviations correspond to IMA-CNMNC

723   approved symbols: kln – kaolinite, alu – alunite, py – pyrite, mrc – marcasite, mnt –

724   montmorillonite, brt – barite, qz – quartz, ms – muscovite, dck – dickite, ilt – illite, prl –

725   pyrophyllite, dsp – diaspore, trd – tridymite, ab – albite (Warr, 2021). Abbreviations without

726   IMA approved symbols: adl – adularia, cldy – chalcedony.

727   Figure 3: Feldspar ternary diagram showing distribution of feldspar populations based on mode

728   of occurrence and unaltered samples from Pritchard and Larson, 2012. Solid circle, unaltered

729   samples, fall into two grouping - potassium feldspar and calcic plagioclase. Phenocryst samples

730   from altered rock largely fall into similar groupings. Devitrification products, grains found as

731   subhedral to euhedral open-space filling, fall in the unaltered sanidine cluster with two outliers as

732   potassium enriched samples. Secondary grains, analyses from grains that grew in veins, are

733   primarily found in the cluster near the orthoclase end member with a few examples in the

734   primary sanidine cluster.

735   Figure 4: Orthoclase percent and wt% BaO from EPMA on feldspar crystals with grain

736   distribution based on mode of occurrence. Unaltered phenocryst samples from Pritchard and

737   Larson, 2012 fall in two groups, one less than 20% orthoclase (plagioclase) and one between 40

738   and 60% orthoclase apparently projecting down from about 2.0 wt% BaO. Phenocryst analyses

739   from altered rocks largely follow the same patterns, however, sanidine phenocrysts also form a

740   cluster with less than 0.5 wt% BaO with more scatter in the orthoclase percent than unaltered

741   phenocrysts and an outlier at 80% orthoclase with low BaO. Devitrification products follow the

742   same trend as devitrification products, typically with lower BaO concentrations. Secondary

743   feldspar samples and replaced phenocryst samples cluster above 90% orthoclase with 0 to about

744   1.5 wt% BaO.

745   Figure 5: Backscattered electron image of chemical zonation of a sanidine phenocryst. Brighter

746   areas contain greater amounts of barium.

747   Figure 6: Paragenesis diagram for Seven Mile Hole. The diagram assumes alteration began with

748   alkaline-chloride fluids to produce illite, quartz, and hydrothermal feldspars of adularia,

749   buddingtonite, and hyalophane. Infiltration of acid-sulfate fluids altered the host rock to

750   kaolinite, opal, marcasite, and alunite supergroup minerals. Around the time marcasite

751   deposition stops and pyrite deposition begins, a small period of sphalerite and galena deposition

752   occurred. Late-stage alteration is dominated by kaolinite, opal, and alunite supergroup minerals

753   with native sulfur, barite, and chalcedony as some of the latest minerals to form. Italicized

754   minerals were noted by previous workers but not in the current study.

755   Figure 7A: Sanidine phenocryst entrained in a quartz vein with white pyrite grains near the top of

756   the image. The phenocryst is replaced along irregular boundaries by a lighter gray adularia.

757   Figure 7B: Completely replaced phenocryst. Remaining feldspar islands are adularia. Adularia

758   was replaced by quartz and alunite supergroup minerals. Most of the outermost portions have

759   been altered to darker kaolinite.

760   Figure 7C: Partially replaced adularia in a quartz vein. Adularia was replaced by alunite

761   supergroup minerals that show some zonation, where the outer zone is slightly darker than the

762   interior.

763   Figure 7D: Large patch of alunite supergroup minerals replacing adularia. The remaining

764   feldspar islands are adularia with scattered quartz found around the margins of the alunite

765   supergroup minerals, note the compositional banding in alunite supergroup minerals. The

766   darkest phases are kaolinite replacing the alunite supergroup minerals.

767   Figure 7E: Replaced phenocryst next to a quartz vein. The phenocryst was fractured and quartz

768   replaced the grain along a linear trend. Small adularia islands are potassium rich. The two

769   largest alunite supergroup minerals are mostly rimmed by bright alunite supergroup minerals

770   with a greater Fe component, implying a greater jarositic component.

771   Figure 8: Temperature v log m ([KCl + K+]/[HCl + H+]). White micas are separated into illite

772   and muscovite and kaolin minerals into dickite and kaolinite by the thick dashed lines. The

773   black arrow indicates a potential pathway as fluid chemistry shifted from alkaline-chloride to

774   acid-sulfate. Modified after Hedenquist and Arriabas, 2022.

775   Supplementary Material captions

776   Supplemental Table 1: Whole-rock XRF data. Sample numbers with "A" represent vein samples

777   except for JZ-25A. Both JZ-25 and JZ-25A are siliceous sinter samples with color differences.

778   Samples JZ-26 and JZ-27 are siliceous sinter samples.

779   Supplemental Table 2: Whole-rock ICP-MS data. Sample numbers with "A" represent vein

780   samples except for JZ-25A. Both JZ-25 and JZ-25A are siliceous sinter samples with color

781   differences. Samples JZ-26 and JZ-27 are siliceous sinter samples.

782   Supplemental Table 3: Alunite supergroup mineral analyses. Sample names include brief

783   comments that do not indicate the correct mineral. Mineral formulas and comments are given in

784   far right columns.

785   Supplemental Table 4: Feldspar analyses. Sample names include brief comments that do not

786   necessarily indicate the correct mineral or mode of occurrence. Mineral formulas and comments

787   are given in far right columns.

Fig 1

Fig. 2

Fig. 3

Fig. 5

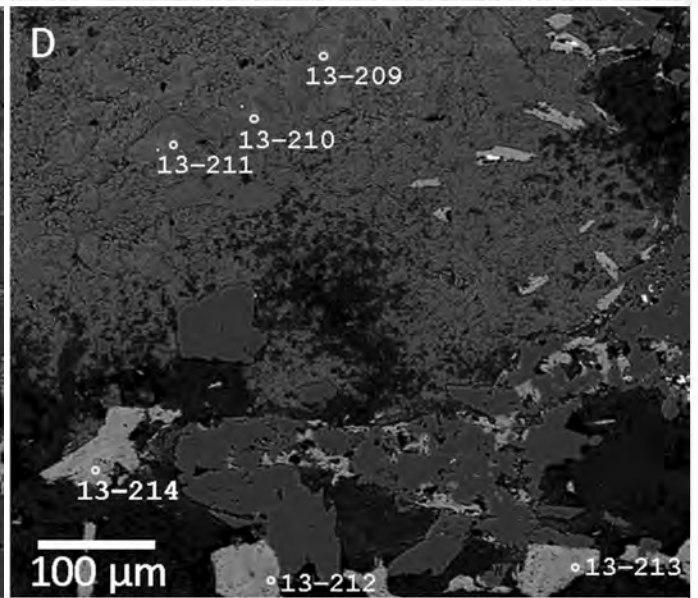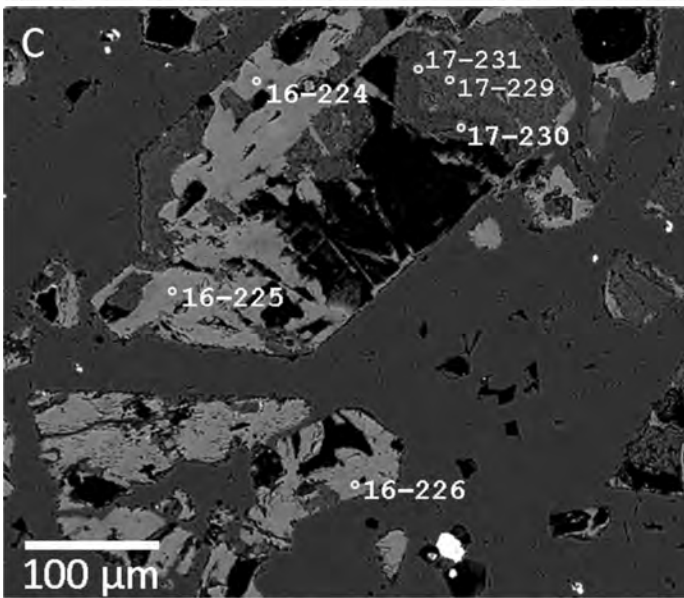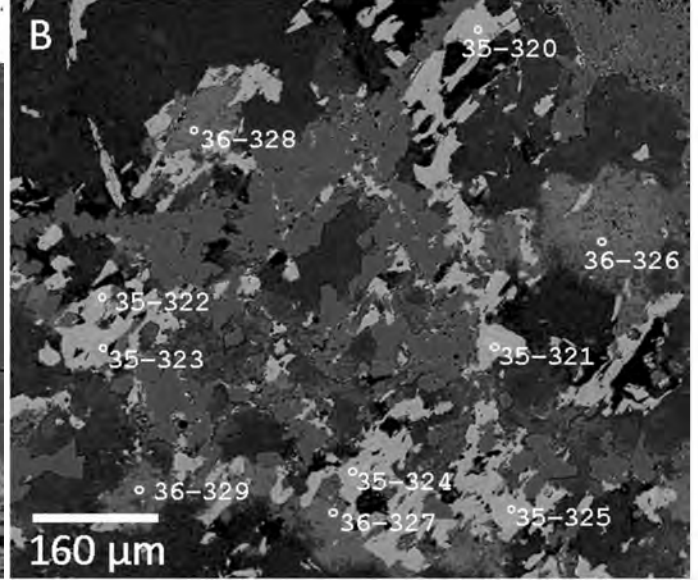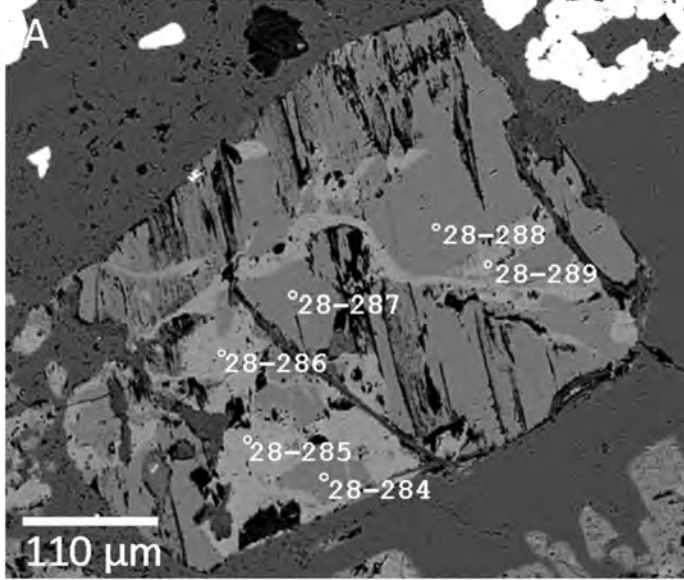|	
Kaolinite	
Illite	
Quartz	
Opal	
Chalcedony	
Marcasite	
Pyrite	
Sphalerite	?? ??
Galena	?? ??
Native Sulfur	??
Adularia	
Buddingtonite	
Hyalophane	
Alunite Supergroup Minerals	
Barite	
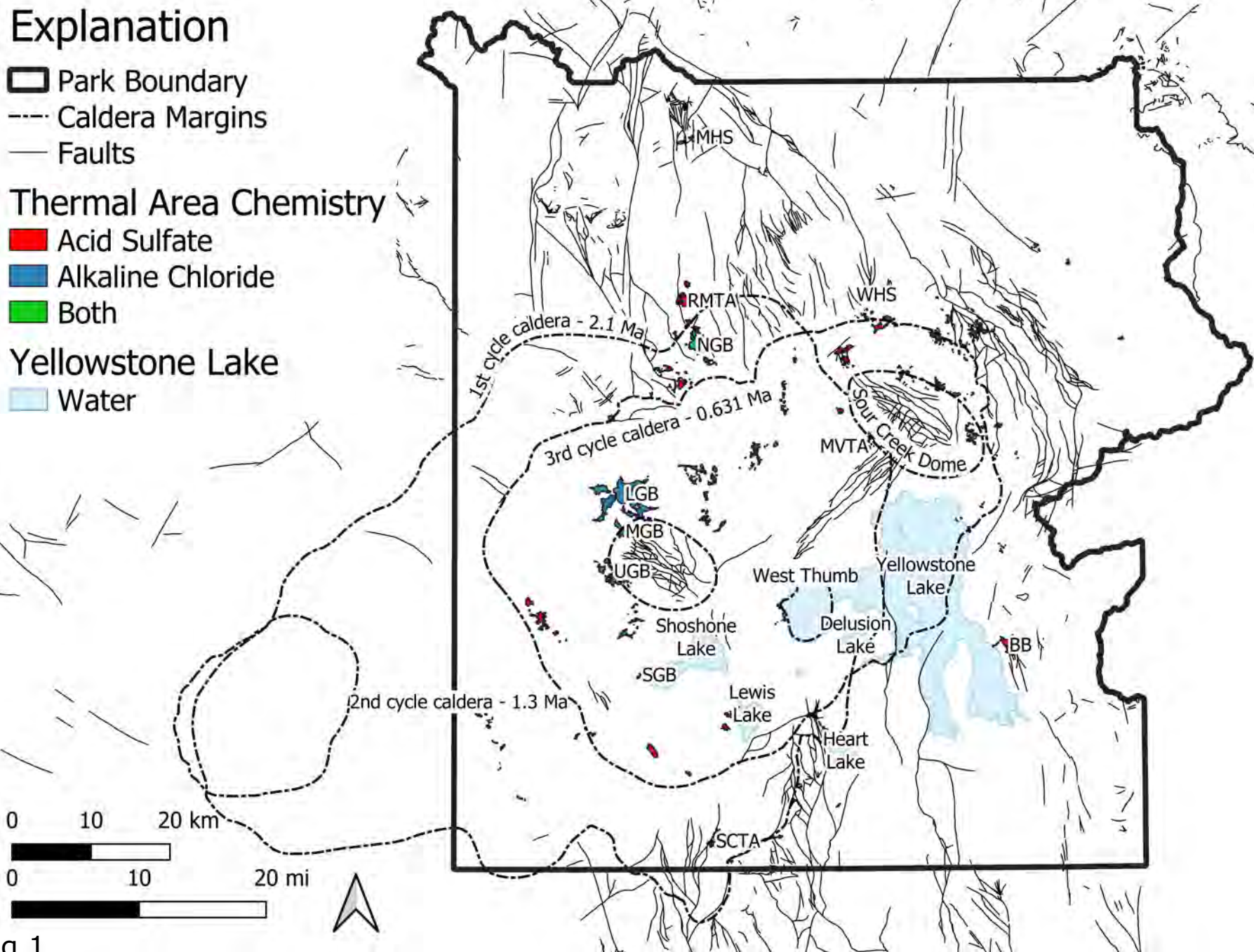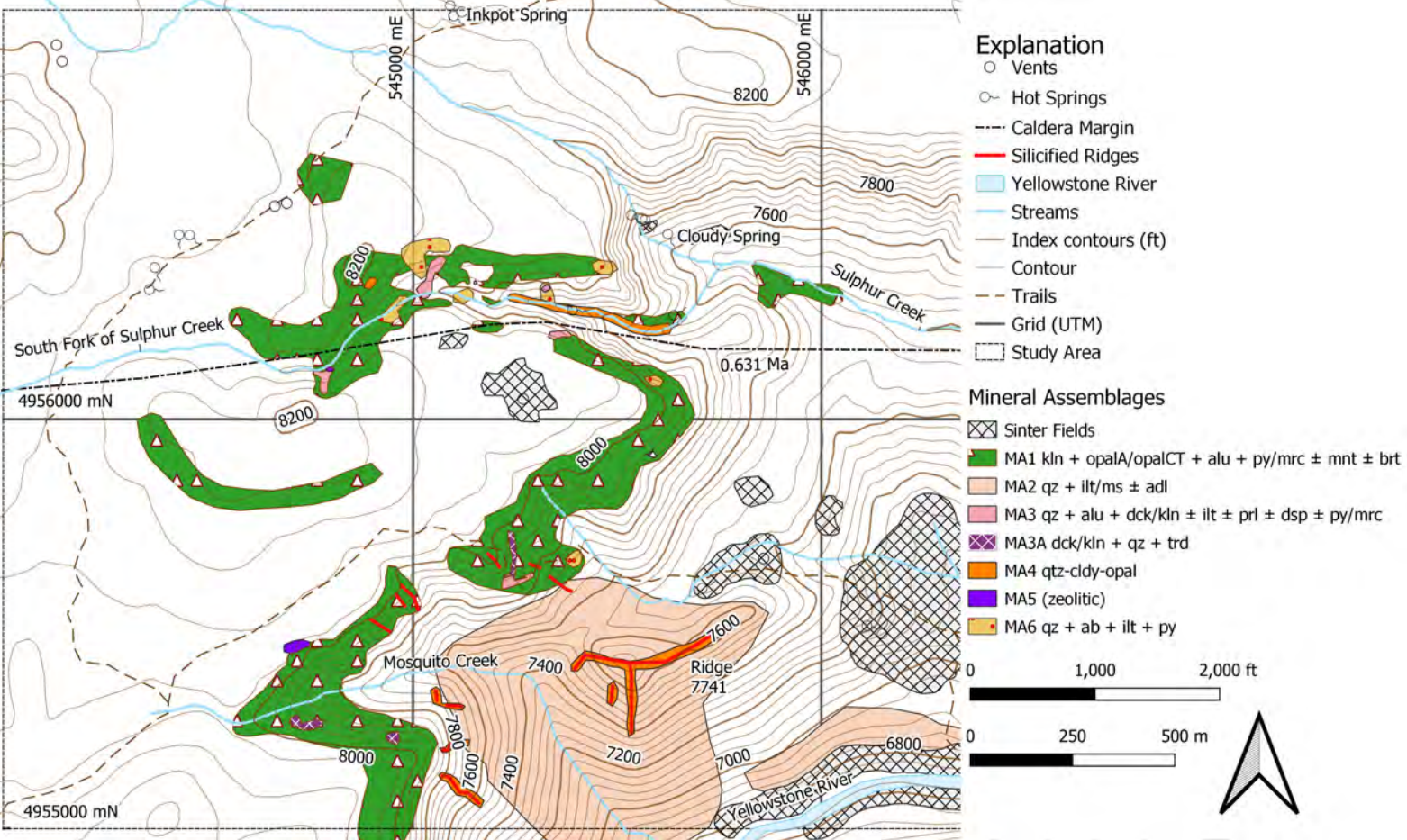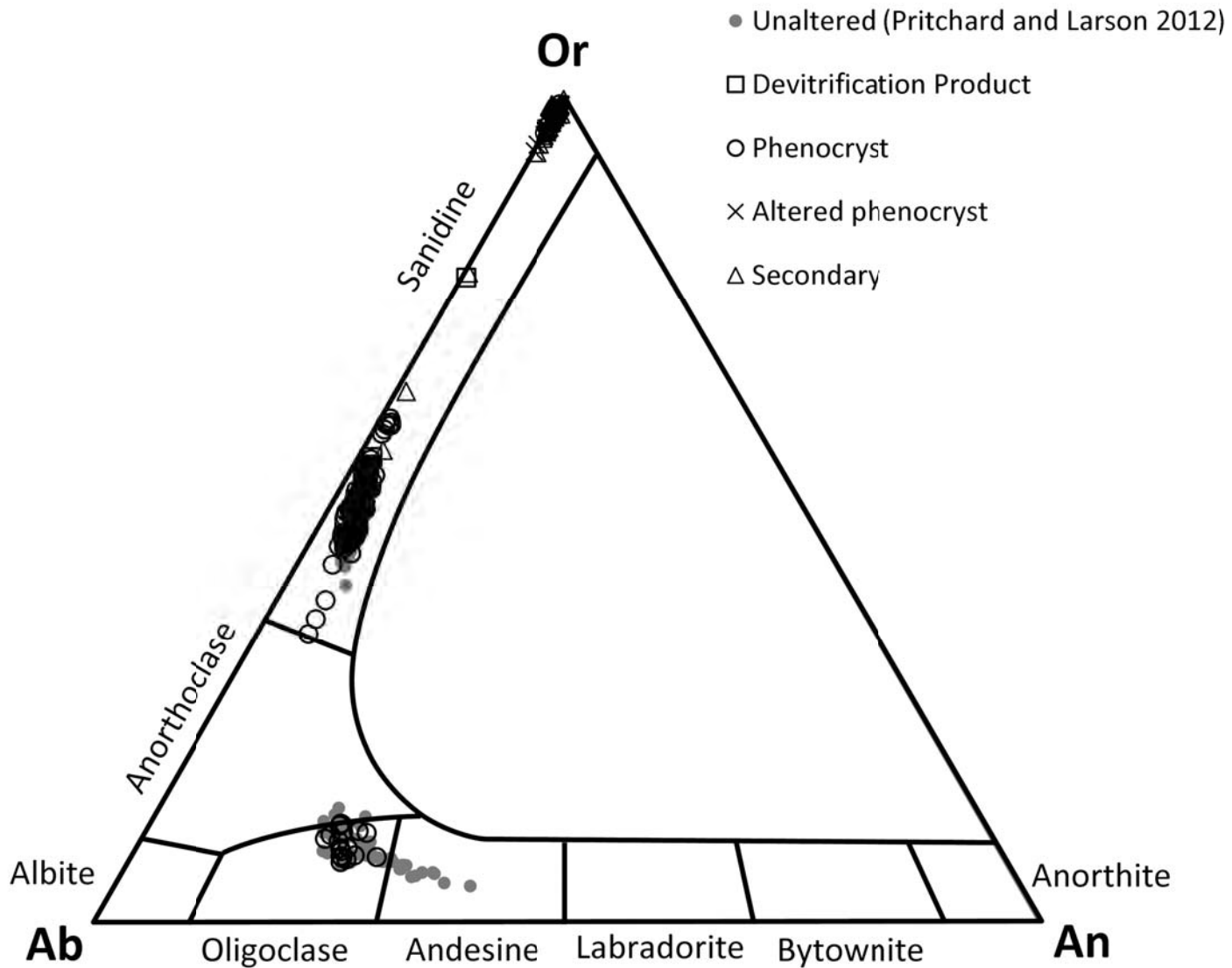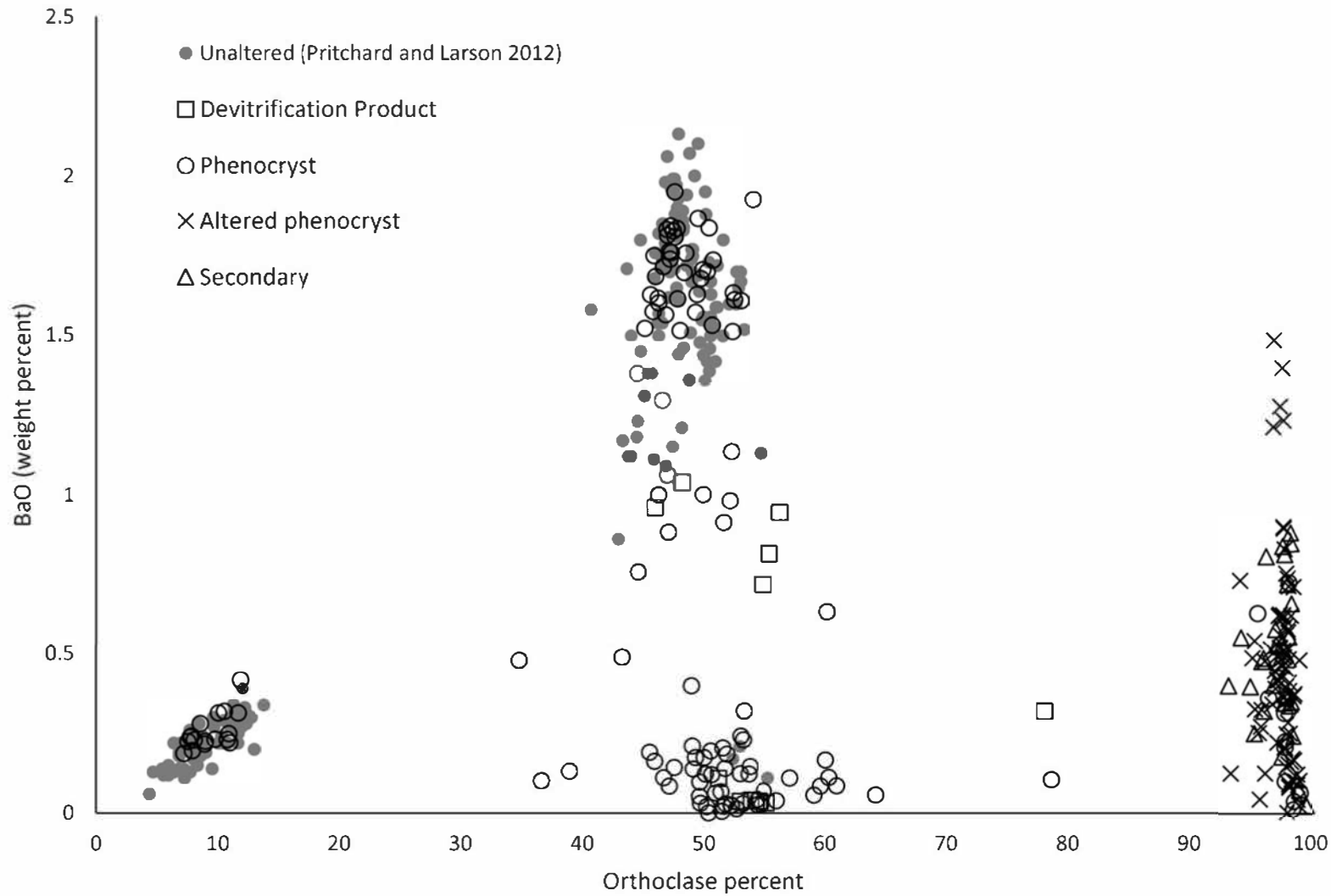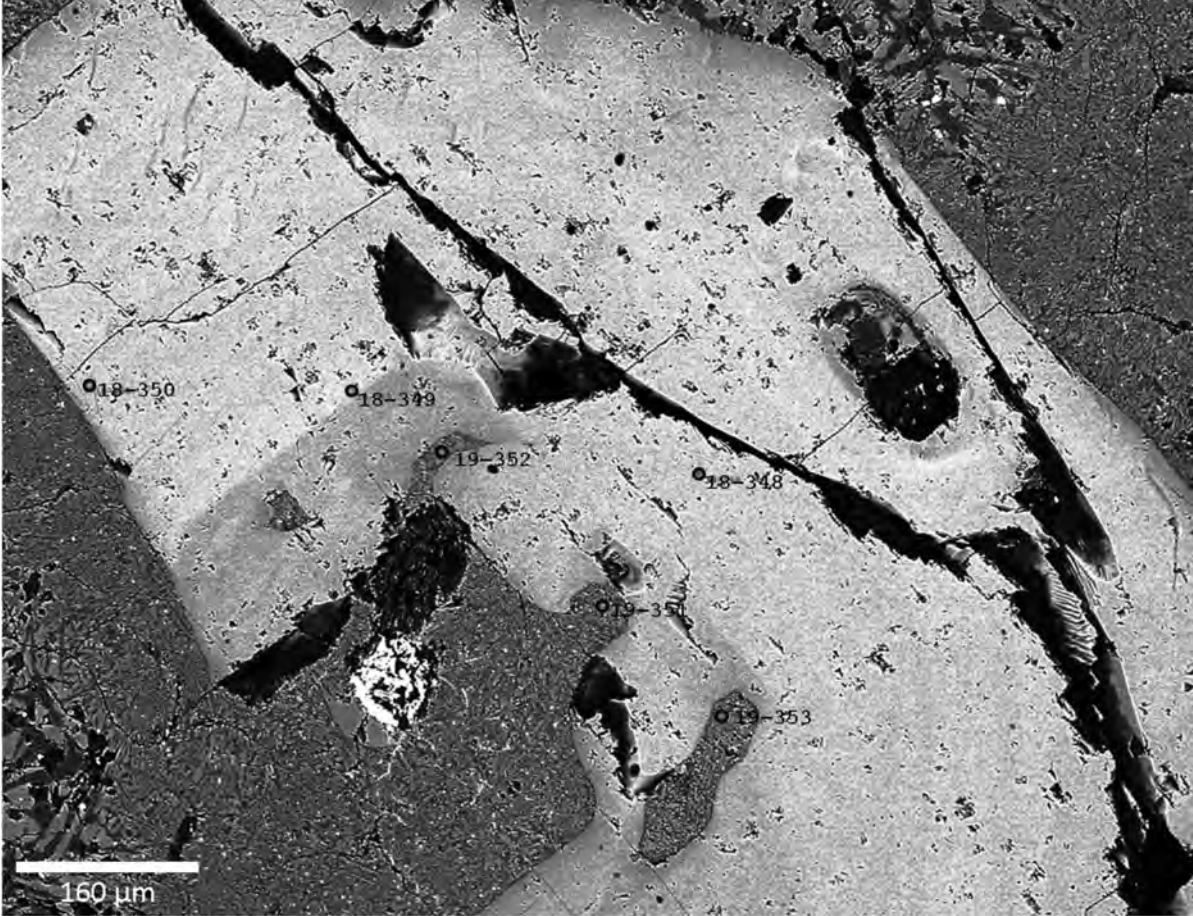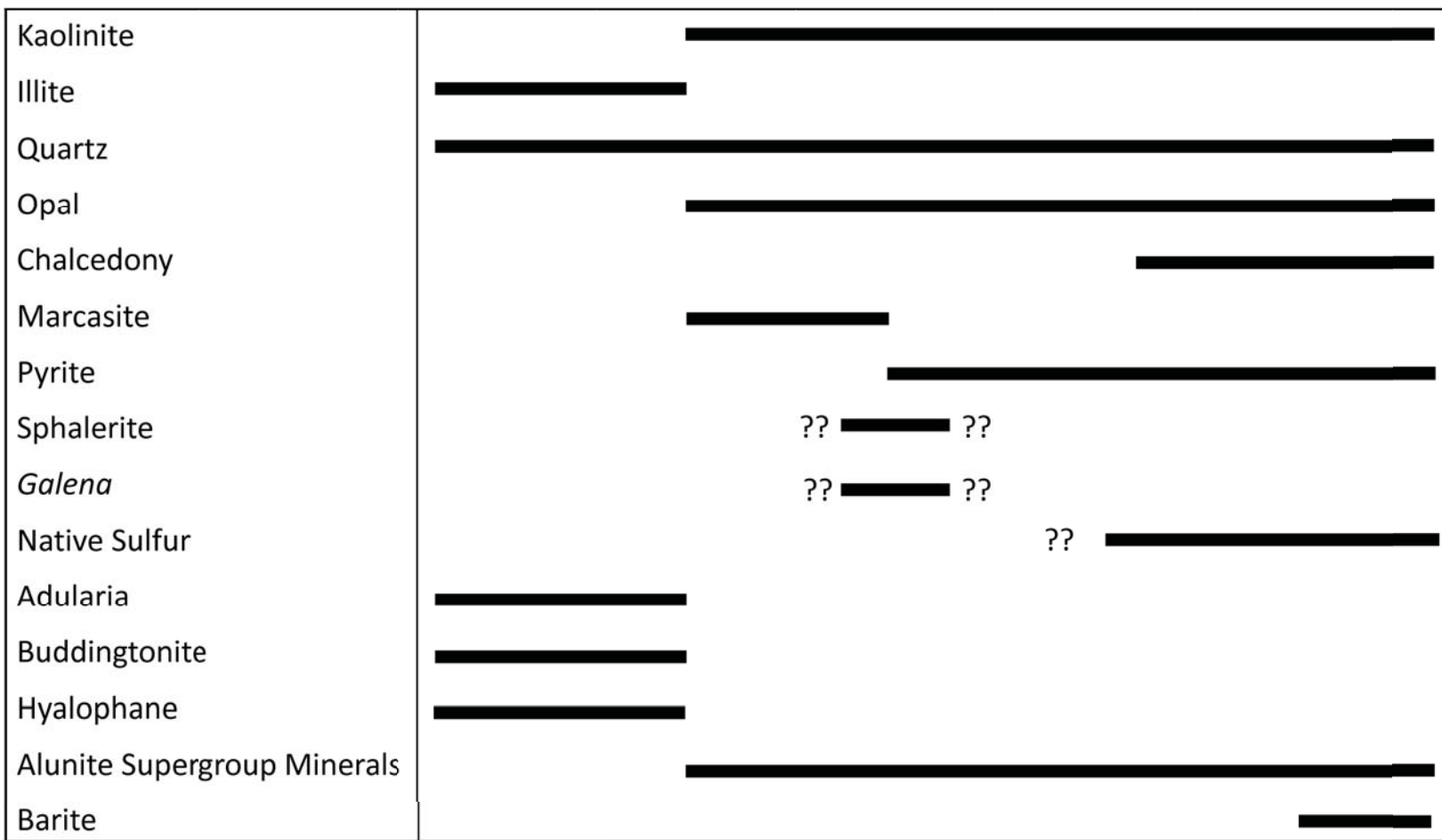
Fig 6
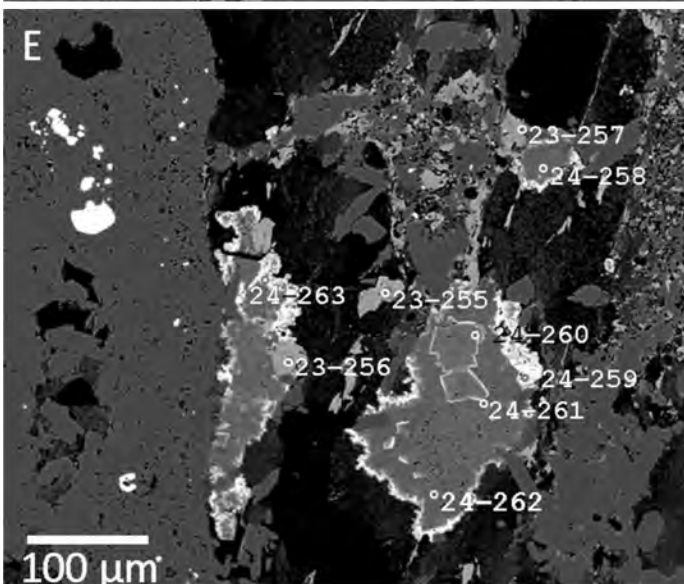
Operating Conditions
Voltage 15 KeV
Current 15 mA
Spot size 5 μm

Fig. 7

Fig 8